

Sub-cloud turbulence explains cloud-base updrafts for shallow cumulus ensembles: First observational evidence

Youtong Zheng¹, Daniel Rosenfeld², and Zhanqing Li³

¹University of Maryland, College Park

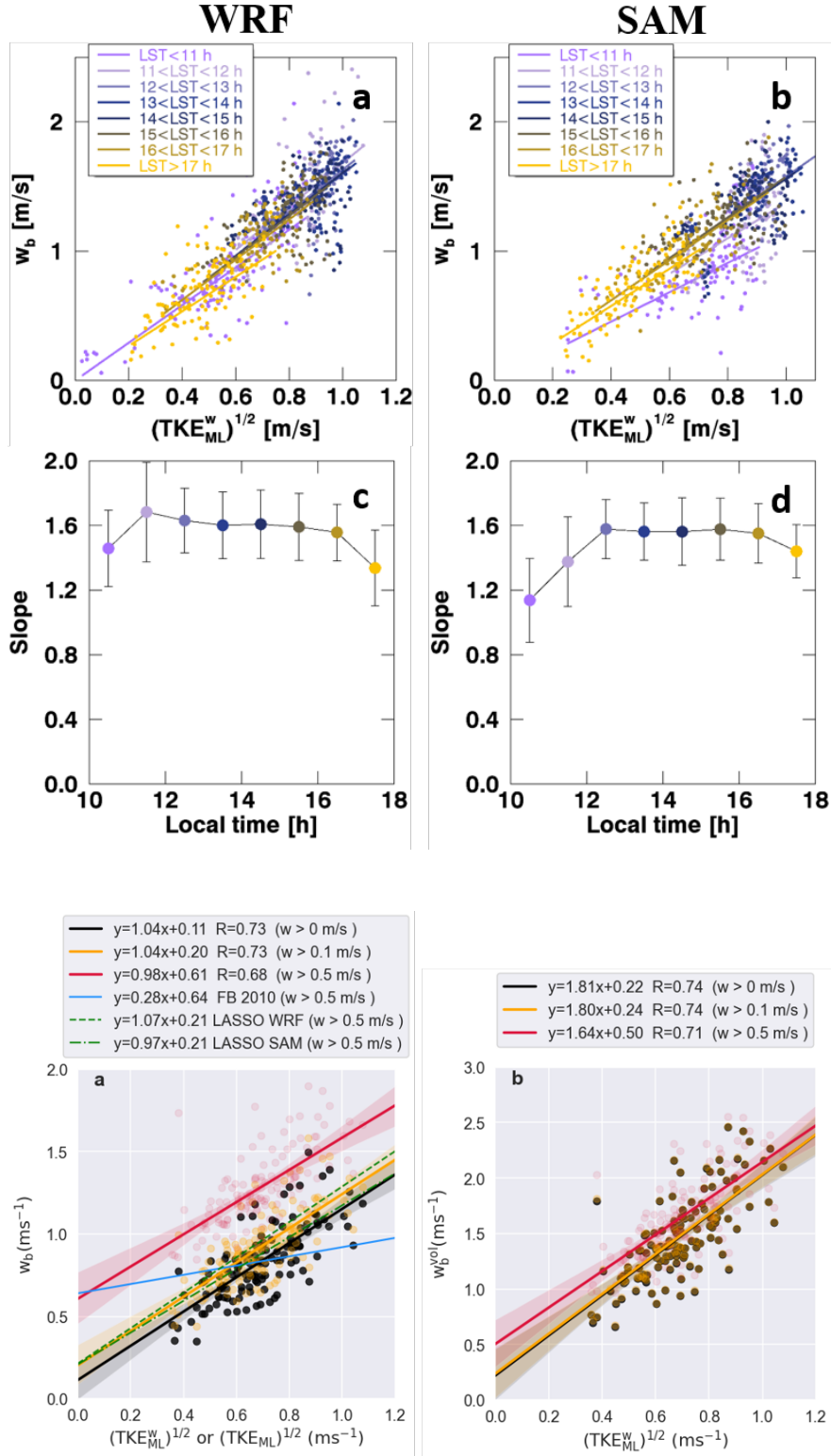
²Hebrew University of Jerusalem

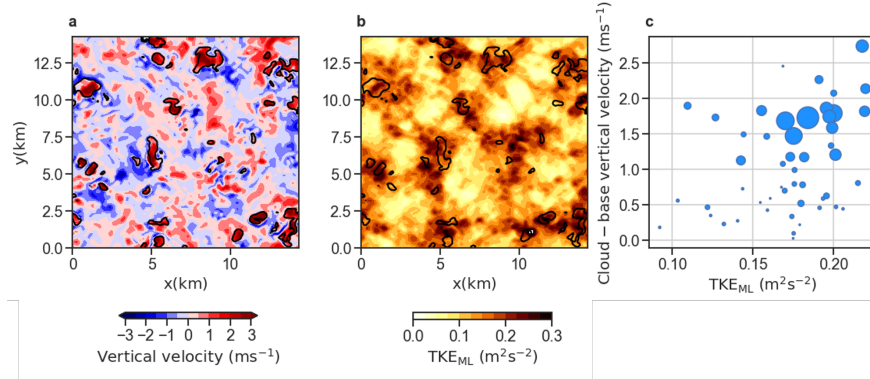
³UMD/ESSIC

November 21, 2022

Abstract

Sub-cloud turbulent kinetic energy has been used to parameterize the cloud-base updraft velocity (w_b) in cumulus parameterizations. The validity of this idea has never been proved in observations. Instead, it was challenged by recent Doppler lidar observations showing a poor correlation between the two. We argue that the low correlation is likely caused by the difficulty of a fixed-point lidar to measure ensemble properties of cumulus fields. Taking advantage of the stationarity and ergodicity of early-afternoon convection, we developed a lidar sampling methodology to measure w_b of a shallow cumulus (ShCu) ensemble (not a single ShCu). By analyzing 128 ShCu ensembles over the Southern Great Plains, we show that the ensemble properties of sub-cloud turbulence explain nearly half of the variability in ensemble-mean w_b , demonstrating the ability of sub-cloud turbulence to dictate w_b . The derived empirical formulas will be useful for developing cumulus parameterizations and satellite inference of w_b .





27 **Abstract**

28 Sub-cloud turbulent kinetic energy has been used to parameterize the cloud-base updraft velocity (w_b) in
29 cumulus parameterizations. The validity of this idea has never been proved in observations. Instead, it was
30 challenged by recent Doppler lidar observations showing a poor correlation between the two. We argue that
31 the low correlation is likely caused by the difficulty of a fixed-point lidar to measure ensemble properties
32 of cumulus fields. Taking advantage of the stationarity and ergodicity of early-afternoon convection, we
33 developed a lidar sampling methodology to measure w_b of a shallow cumulus (ShCu) ensemble (not a single
34 ShCu). By analyzing 128 ShCu ensembles over the Southern Great Plains, we show that the ensemble
35 properties of sub-cloud turbulence explain nearly half of the variability in ensemble-mean w_b ,
36 demonstrating the ability of sub-cloud turbulence to dictate w_b . The derived empirical formulas will be
37 useful for developing cumulus parameterizations and satellite inference of w_b .

38

39

40

41

42

43

44

45

46

47

48

49

50

51

52 1. Introduction

53 Cloud-base updraft velocity (w_b) is a crucially important variable as it influences various
54 aspects of cumulus clouds (Rogers and Yau, 1996). The w_b modulates the aerosol cloud-mediated
55 effect by governing the supersaturation near cloud bases (Twomey, 1959; Rosenfeld, 2014). In
56 polluted conditions, cloud droplet size and number concentration are more sensitive to w_b than
57 aerosol concentration and size (Reutter et al., 2009). Moreover, w_b dictates lateral entrainment of
58 cumulus that remains an unresolved bottleneck for climate modeling (Donner et al., 2016).

59 Despite its importance, current cumulus parameterization schemes rarely express w_b
60 explicitly (Donner et al., 2016). Most schemes parameterize the cloud-base mass flux (M_b) without
61 specifying the w_b . For example, Arakawa and Schubert (1974) determine the M_b by adjusting the
62 cloud work function towards a value maintaining an equilibrium between the large-scale forcing
63 and the convection. Krishnamurti et al. (1983) determine M_b under the assumption that convection
64 must balance the column integrated vertical advection of moisture. Kain and Fritsch (1993) and
65 Grell (1993) parameterize M_b by requesting the convection to remove the large-scale instability
66 over the convective time scale.

67 The earliest effort that explicitly represents the w_b in M_b closure is Brown (1979) who
68 approximates the w_b using the environmental vertical velocity from the surrounding nine points at
69 lower tropospheric levels. This scheme is physically flawed by the fact that the air masses that
70 initiate cumulus clouds are convective in nature. This issue is addressed by Neggers et al. (2009)
71 and Fletcher and Bretherton (2010) (FB10) who argued that the w_b could be dictated by the sub-
72 cloud turbulent intensity. FB10 used a set of cloud-resolving simulations to empirically derive the
73 following formula to represent the w_b :

$$74 \quad w_b = 0.28 \times \text{TKE}_{\text{ML}}^{1/2} + 0.64, \quad (1)$$

75 in which the TKE_{ML} is the turbulent kinetic energy averaged horizontally and vertically in the sub-
76 cloud mixed layer. FB10 shows that such a boundary-layer-based mass flux closure scheme
77 outperforms several commonly used schemes for three cumulus cases.

78 Still lacking is observational evidence of the ability of TKE_{ML} to explain the w_b . As quoted
79 by Donner et al. (2016): “... *parameterizations that do provide vertical velocities have been*

80 *subject to limited evaluation against what have until recently been scant observations.*” The only
81 observational pursuit to evaluate the Eq. (1) is from Lareau et al. (2018) who analyzed Doppler
82 lidar observations of ~1500 individual shallow cumulus (ShCu) over the Southern Great Plains
83 (SGP), finding that sub-cloud vertical velocity variance (a proxy for TKE_{ML}) explains only a few
84 percent of the w_b variability. This led them to cast doubt upon the relationship. They argue that
85 sub-cloud updrafts must work against negative buoyancy near the top of the mixed layer to
86 generate w_b , and such a penetrative nature of the convection deteriorates their correlations.

87 Given the contrasting results, it is imperative to answer the question of whether or not sub-
88 cloud turbulence explains the w_b . This is not only important for cumulus parameterizations but
89 also crucial for advancing other pursuits in the field of cumulus dynamics. First, theoretical
90 inquiries of cumulus dynamics often rely on the assumption of a tight coupling between the sub-
91 cloud turbulence and w_b . For example, in one-dimensional bulk models of boundary layer clouds,
92 a key variable is the Deardoff velocity scale, w^* , which dictates the sub-cloud turbulence intensity
93 (Betts, 1973; Neggers et al., 2006; Stevens, 2006; Zheng, 2019). Linking the w^* with the w_b is the
94 basis for several important coupling processes between the cloud and sub-cloud layers (Neggers
95 et al., 2006; van Stratum et al., 2014; Zheng et al., 2020). Second, recently emerging new satellite
96 remote sensing methodologies of retrieving w_b (Zheng and Rosenfeld, 2015; Zheng et al., 2015,
97 2016) have offered great insights into the aerosol indirect effect and climate change (Rosenfeld et
98 al., 2016; Seinfeld et al., 2016; Li et al., 2017; Grosvenor et al., 2018; Rosenfeld et al., 2019).
99 These studies infer the w_b via quantifying the TKE_{ML} or its equivalents. Evaluating if the TKE_{ML}
100 explains the w_b is essential to evaluate the physical validity of these techniques.

101 To that end, this study examines the relationship between the w_b and sub-cloud turbulence
102 for ShCu using DL observations over the SGP. We focus on w_b of ShCu ensembles, not single
103 ShCu, because the former is more relevant to cumulus parameterization. We show that ensemble-
104 averaged w_b and sub-cloud turbulence are highly correlated with statistical significance
105 (correlation coefficient greater than 0.7). Evaluating the relationship on ensembles but not on
106 individual ShCu might explain the disparities with the previous finding (Lareau et al., 2018). The
107 next session discusses the difference between the ensemble-mean w_b and the w_b of single cumuli.
108 It lays the foundation for developing the sampling strategy of ShCu ensembles. Section 3

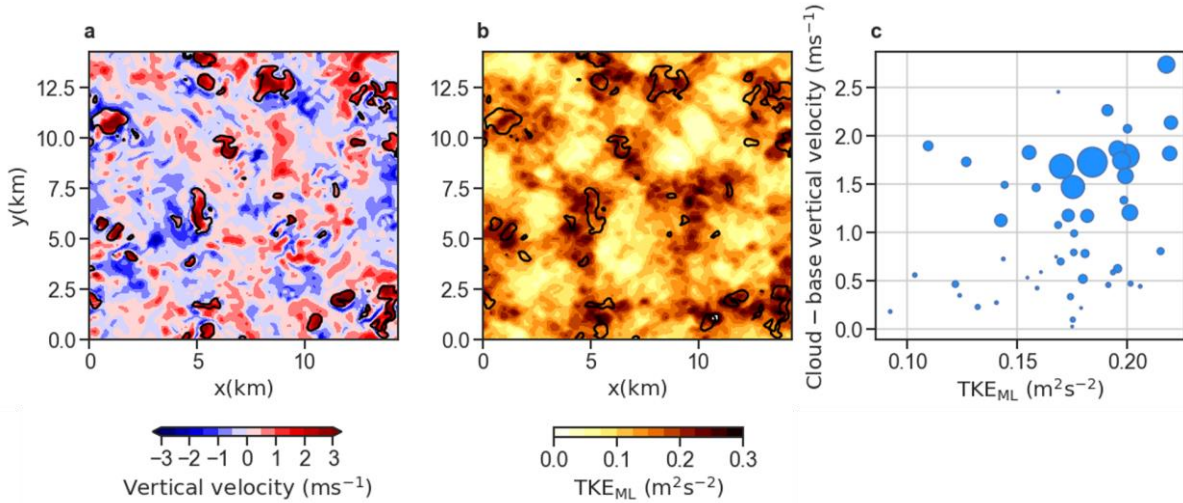
109 introduces the observational data and methodology. Section 4 shows the results, followed by a
110 summary.

111

112 2. w_b of cumulus ensembles

113 Distinguishing between the ensemble and individual ShCu is necessary. The concept of
114 cumulus ensemble is a fundamental building block for all cumulus parameterizations (Arakawa
115 and Schubert, 1974). A cumulus ensemble on spatial scales of several tens of kilometers is
116 composed of individual cumulus with a wide range of distributions in size and age. Since the
117 individual cumulus clouds are at different stages of their lifetime, their physical properties differ
118 considerably even if the surface and large-scale forcing are uniform.

119 The difference could be illustrated by Figure 1 showing a ShCu ensemble simulated by the
120 Weather Research and Forecasting (WRF) in the Large-Eddy Simulation (LES) Atmospheric
121 Radiation Measurements (ARM) Symbiotic Simulation and Observation (LASSO) project (Text
122 S1). The surface fluxes and large-scale forcing are uniform over the 14.4×14.4 km domain with
123 a horizontal grid size of 100 m. The vertical velocity field at the cloud-base level shows a
124 distinctive pattern with strong updrafts within clouds surrounding by shells of downdrafts (Fig.
125 1a). We can see a rough correspondence between the vertical velocity field at the cloud-base level
126 (Fig. 1a) and the TKE_{ML} (Fig. 1b): regions with larger TKE_{ML} typically have stronger updrafts
127 near cloud bases. Such a correspondence, however, breaks down on the length scale of a single
128 ShCu. For example, the vertical velocity field shows strong updrafts within individual clouds
129 surrounding by shells of downdrafts whereas the TKE_{ML} variability across the cloud edges is
130 considerably more uniform. This is not surprising since both updrafts and downdrafts contribute
131 to the vertical mixing, jointly regulating the TKE_{ML} . As a result, their covariation on the length
132 scale of individual ShCu tends to be noisy, which is confirmed by Figure 1c that compares the two
133 quantities averaged over individual ShCu. The degree of scattering is likely to increase
134 substantially when the synoptic and surface forcings are allowed to change.



135

136

137 **Figure 1:** Examples of the different length scales of spatial variability of w_b and TKE_{ML}

138 using WRF-simulated ShCu on 21 UTC, June 6, 2015. (a) Spatial distribution of vertical velocity

139 at the cloud-base level with maximum cloud coverage. Black contours mark the cloudy regions

140 with liquid water content greater than 0.01 g/m^3 . (b) The same scene but the color shading is the

141 TKE_{ML} . (c) Scatter plot of cloud-base vertical velocity versus TKE_{ML} , with each point

142 representing mean over individual cumuli. The size of a point is proportional to the size of

143 cumuli. The data are obtained from the first phase of LASSO project. The TKE_{ML} is computed as

$$0.5(u'^2 + v'^2 + w'^2) \text{ averaged below the cloud base.}$$

144

145

146

147

148

149

150

151

152

153

154

Measuring the ensemble-mean w_b from a surface-based DL, however, is challenging. The DL at a fixed location samples a line of cloud elements along the direction of horizontal winds. In order to sample an adequate amount of individual cumuli to constitute an ensemble, the sampling time window must be at least several hours. For example, for the wind speed of 5 m/s, a 2-hour sampling window corresponds to a distance of $\sim 36 \text{ km}$, comparable to the spatial scale of a continental ShCu ensemble. However, ShCu experiences distinctive diurnal variations over the continent. Within the 2-hour sampling period, the ShCu ensemble may evolve, leading to sampling uncertainties. Fortunately, a convective boundary layer often experiences a quasi-steady state (Moeng, 1984; Lensky and Rosenfeld, 2006; Stull, 2012). In atmospheric science, whether a dynamical system can be considered quasi-steady depends on the difference between the

155 characteristic time scale of the system and the time scale of external forcing. For a typical
156 convective boundary layer over the continent, the surface forcing time scale is on the order of a
157 few hours (defined as half of the period when the surface heat fluxes remain positive) whereas the
158 time scale for shallow convective circulations is several tens of minutes (i.e. the convective time
159 scale) (Fig. S1a). Such a time scale separation allows the mixed layer to remain in a quasi-steady
160 state in which changes in turbulent properties are negligible compared with the turbulence
161 production and dissipation terms (Stull, 2012). This quasi-steady assumption is particularly valid
162 in the early afternoon when the surface fluxes reach their plateau and their time derivatives
163 minimize (Fig. S1b). As such, focusing on early-afternoon ShCu can reduce the uncertainty of
164 sampling due to temporal evolution.

165 In summary, to measure the w_b of ShCu ensembles from surface-mounted DL, the sampling
166 window must be at least a few hours to sample enough amount of individual ShCu. Moreover, an
167 ideal sampling period is the early afternoon when the boundary layer is close to stationarity.

168

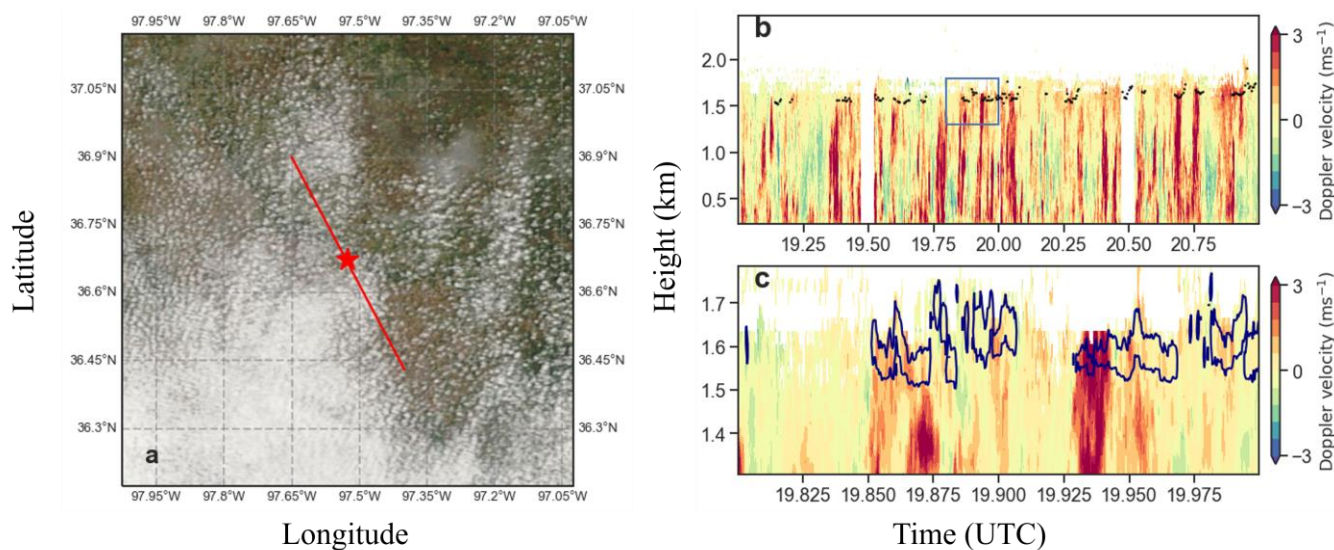
169 **3. Data and Methodology**

170 We use observations from the Department of Energy's Atmospheric Radiation
171 Measurements (ARM) SGP observatory. The key instrument used in this study is the DL. The DL
172 measures vertical velocity with ~ 1 s temporal and 30 m vertical resolution. The transmitted
173 wavelength is 1.5 μm . In addition to DL, we also use data from radiosondes, a ceilometer, a Ka-
174 band cloud radar (KAZR), and ARM instruments measuring surface meteorological variables
175 routinely.

176 **3.1. An example case**

177 To illustrate the sampling principle of ShCu ensembles, Figure 2a shows a MODIS satellite
178 imagery of a ShCu field over the SGP at 20:30 UTC on June 10, 2012. The wind is southeasterly
179 at a speed of ~ 9 m/s, corresponding to a horizontal distance of ~ 70 km over the two hours (the
180 red solid line in Fig. 2a). One can see a few dozens of single cumuli drifting over the SGP site
181 along the wind direction. Figure 2b shows a time-height plot of the DL from 19 to 21 UTC,
182 corresponding to 13 \sim 15 local standard time (LST). Black dots mark the cloud-base heights (z_b)

183 measured by the ceilometer. To count how many individual cumuli are sampled during this period,
 184 we use the DL reflectivity to identify single cumuli. Figure 2c shows the zoomed-in window near
 185 cloud bases during the 19:48 ~ 20:00 UTC. The navy contours encompass pixels with DL
 186 reflectivity greater than $10^{-4.6} \text{ m}^{-1} \text{ sr}^{-1}$, a threshold that defines cloudy pixels (Lareau et al., 2018).
 187 Based on the reflectivity threshold, a total of 84 individual clouds are identified during the 2-h
 188 period. The majority of them have a duration shorter than 4 s, which seems too short to constitute
 189 a single cloud. Thus, we conglomerate clouds with gaps < 20 s, reducing the cloud population to 29,
 190 with 12 of them lasting longer than 30 s.



191

192 **Figure 2:** An example case of the shallow cumulus field on Jun 10, 2012, over the SGP.

193 (a) MODIS image centered on the SGP site (red star) at ~20:30 UTC. The red solid line
 194 marks the rough direction and travel distance of the mean horizontal wind during the 19 ~
 195 21 UTC. (b) Height-time plot of Doppler lidar image of vertical velocity during a two-
 196 hour window from 19 to 21 UTC. The black dots mark the cloud-base heights measured
 197 by a ceilometer. The blue rectangle marks a smaller window shown in the (c). Navy
 198 contours mark the cloudy regions defined as groups of pixels with reflectivity greater
 199 than $10^{-4.6} \text{ m}^{-1} \text{ sr}^{-1}$.

200

201

202 3.2. Computing the w_b

203 We select “cloud-base” DL pixels through two steps. First, to exclude the decoupled cloud
204 elements and elevated cloud sides, pixels with cloud bases higher than 30% of lifting condensation
205 level (LCL) are removed. Second, for the remaining coupled clouds, we select pixels within three
206 gates below the cloud base (~ 100 m) and cloudy pixels above the cloud base. These pixels are
207 defined as “cloud-base” pixels. Because of the strong signal attenuation, the DL only penetrates $<$
208 100 m into the clouds. Therefore, the cloudy pixels are mostly concentrated near several tens of
209 meters above the cloud base. Figure S2 shows a comparison of the vertical velocity probability
210 density function (PDF) between the two sub-groups of “cloud-base” pixels. Their PDF
211 distributions are overall similar, suggesting that it is tenable to combine them as “cloud-base”
212 pixels.

213 To compute the ensemble-mean w_b , we average the selected vertical velocities in two ways.
214 The first is to simply average the vertical velocities above a threshold: $\bar{w} = \sum N_i w_i / \sum N_i$, in which
215 the N_i represents the frequency of occurrence of positive vertical velocity w_i that is greater than a
216 critical value (w_{crit}). This is the common way for cloud-base mass fluxes study. The second way
217 of averaging is weighted by volume: $\bar{w}^{vol} = \sum N_i w_i^2 / \sum N_i w_i$. The volume-averaged updraft speed
218 has been considered as more relevant to the understanding of aerosol cloud-mediated effects
219 because it gives more weight to the larger vertical velocities that generate clouds with greater
220 volume (Rosenfeld et al., 2014; Zheng et al., 2015; Rosenfeld et al., 2016).

221 3.3. Other quantities

222 Ideally, the TKE_{ML} should be computed as $0.5(u'^2 + v'^2 + w'^2)$ averaged below the cloud
223 base. However, the DL can only measure the vertical component, $0.5w'^2$, denoted as TKE_{ML}^w . In
224 this study, we use the TKE_{ML}^w to approximate the TKE_{ML} , motivated by the fact that TKE_{ML}^w
225 dominates the TKE_{ML} in typical convective boundary layers (Stull, 2012). The potential
226 contributions from horizontal components of TKE_{ML} will be taken into account in our analyses in
227 section 3.

228 We used the surface-measured temperature and moisture to compute the LCL using the exact
229 analytical formula of Romps (2014). As described in the example case, we used the threshold of

230 DL reflectivity to identify single cumuli. To compute the chord length of individual cumuli, we
231 used the DL product of horizontal wind speed near cloud-base, which is derived from a velocity
232 azimuth display algorithm (Teschke and Lehmann, 2017). The multiplication of cloud-base
233 horizontal wind speed and cloud duration yields the cloud chord length.

234 3.4. Case selection

235 A total of 128 ShCu days were selected between 2011 ~ 2014. The selection criterion is in
236 principle similar to previous studies (Zhang and Klein, 2013; Lareau et al., 2018), which involves
237 both objective and subjective criteria. The objective criteria include three steps: (1) the cloud-base
238 height (defined as the mean of the lowest quartile within the 2-h period) has to be within 30% of
239 LCL to ensure coupling, (2) the KAZR reflectivity cannot exceed 0 dBZ between the surface and
240 cloud base to ensure no considerable precipitation, and (3) the cloud duration cannot exceed 30
241 min to exclude stratiform clouds. Besides, we examine KAZR imageries to ensure ShCu-like
242 characteristics. This is the best we can do since a completely objective method for selecting ShCu
243 remains missing, although the emerging new technique of machine learning is promising to
244 address this issue in the near future (Rasp et al., 2019).

245 Based on these criteria, we obtain 32 ShCu days per year, similar to the 28 ShCu days per
246 year in Zhang and Klein (2013) and Lareau et al. (2018), suggesting that there is no marked
247 sampling difference between this study and previous ones. Fig S3 shows the statistics of these
248 selected ShCu ensembles. On average, each ensemble is composed of ~ 20 individual ShCu, with
249 half lasting longer than 30 secs. The majority of the ensembles have the maximum cloud chord
250 length shorter than 5 km, consistent with prior knowledge.

251

252 4. Results

253 4.1. Sub-cloud turbulence explains cloud-base updrafts

254 Figure 3 shows the scatter plots of $\overline{w_b}$ (a) and $\overline{w_b^{vol}}$ (b) versus $(TKE^w_M)^{1/2}$ for different w_{crit} .
255 Overall, the $(TKE^w_M)^{1/2}$ is a good predictor of cloud-base updrafts, explaining ~ 50% of their
256 variabilities. Note that the degree of scattering is still noticeable, but given the instrument error of
257 the DL (~ 0.1 m/s) and potential sampling errors due to the assumption of stationarity, such degrees

258 of correlation are good enough for demonstrating the physical validness. To our knowledge, this
259 is the first observational evidence supporting the ability of the sub-cloud turbulence to dictate
260 cloud-base updrafts that was only found in high-resolution models (Grant and Brown, 1999;
261 Fletcher and Bretherton, 2010; van Stratum et al., 2014). Such good correlations suggest a
262 continuity of vertical momentum between the sub-cloud layer and cloud base, despite the in-
263 between weakly stable layer (i.e. cloud-base transition layer) (Neggers et al., 2007; Stevens, 2007).
264 Indeed, the stability of the transition layer interacts with the convective circulation, a manifestation
265 of the dynamical coupling between the sub-cloud and cloud layers, to reach an equilibrium that
266 maintains the mass conservation (Neggers et al., 2006; Fletcher and Bretherton, 2010). In this
267 regard, the transition layer property should not be considered an external forcing that alters the
268 coupling between the sub-cloud and cloud-base dynamics, but an internal parameter that responds
269 to the circulation.

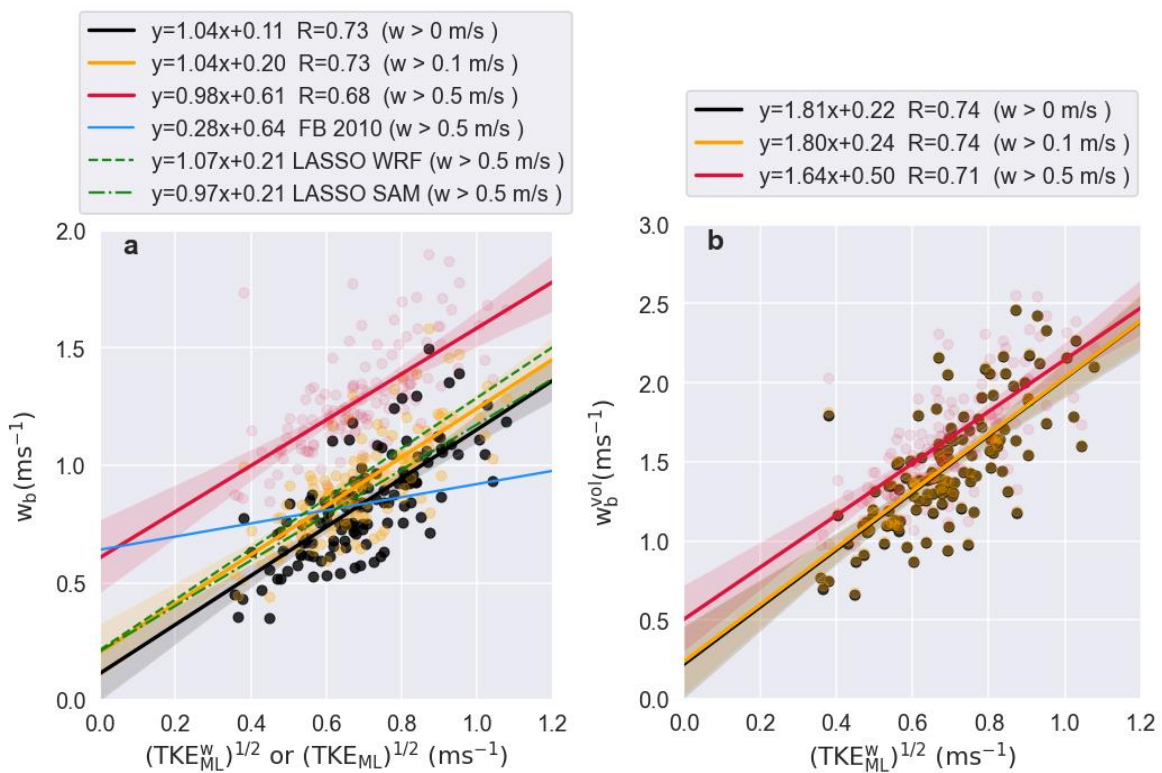
270 Both $\overline{w_b}$ and $\overline{w_b^{vol}}$ increase with the w_{crit} , but the $\overline{w_b^{vol}}$ shows much weaker sensitivity
271 primarily because the $\overline{w_b^{vol}}$ gives more weight to the larger vertical velocities. The intercepts also
272 increase with w_{crit} , which is an artificial consequence of using non-zero w_{crit} . Physically speaking,
273 a zero TKE_M^w should lead to zero cloud-base updraft speed. Therefore, we will focus our
274 subsequent discussions on the slopes that bear more physical meaning than intercepts.

275 To compare our results with that from FB10, we visualize the Eq. (1) in Figure 3a (light blue
276 curve). FB10 uses the w_{crit} of 0.5 m/s. Our empirical estimate (the red line) shows a stronger
277 sensitivity of $\overline{w_b}$ to the sub-cloud turbulence than FB10 by more than a factor of 3. What causes
278 the difference? One possible reason is that we used the TKE_M^w that does not include the horizontal
279 components of the TKE, leading to smaller values of TKE and, thus, a steeper slope. Another more
280 likely reason is that the horizontal resolutions of the model used by FB10 are too coarse (1 km) to
281 accurately simulate the vertical velocities. For instance, modeled vertical velocities decrease with
282 the model resolution by a power law of $-2/3$ (Rauscher et al., 2016; Donner et al., 2016). The
283 underestimated $\overline{w_b}$ due to low resolution may flatten the slope of $\overline{w_b}$ versus $(\text{TKE}_{ML})^{1/2}$ in FB10.

284 To understand which factor is responsible, we use the LES data of 18 ShCu days from the
285 LASSO project (Text S1). The LASSO horizontal resolution is 100 m, 10 times finer than that
286 used in FB10. With the model output of three-dimensional winds, we are able to diagnose the full

287 components of TKE_{ML} so that we can conduct an “apple-to-apple” comparison between the
 288 LASSO and FB10. As shown by the green lines in Fig. 3a, LASSO models (WRF and System for
 289 Atmospheric Modeling, SAM) show slopes steeper than the FB10 by more than a factor of 3 (see
 290 Fig. S4 for their scatter plots with statistical details). This confirms that the flatter slope of FB10
 291 is likely caused by the coarse model resolution. The comparison between the LASSO and DL,
 292 which is not the focus of this study, is discussed in the supplementary material (Text S2).

293 We have tabulated the empirical formulas for $\overline{w_b}$ and $\overline{w_b^{vol}}$ for different w_{crit} (Table S1) so
 294 that readers can use what suits their research interests.



295
 296 **Figure 3:** Scatter plots of $\overline{w_b}$ (a) and $\overline{w_b^{vol}}$ (b) versus $(TKE_{ML}^{w_M})^{1/2}$ for $w_{crit} = 0, 0.1, \text{ and } 0.5$ m/s. Each
 297 point represents a ShCu ensemble mean. The blue solid line marks the Eq. (1), the empirical
 298 formula developed in Fletcher and Bretherton (2010).

299

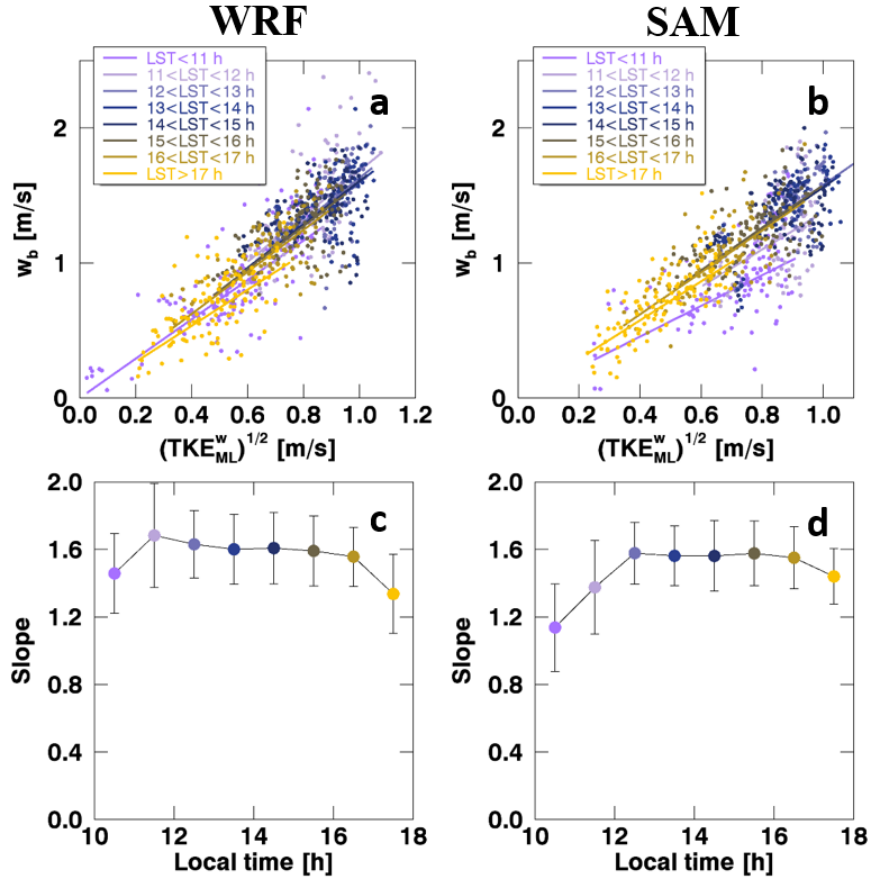
300

301

302 4.2. Diurnal dependence

303 Given that all cases are in the early afternoon, one may ask how the observed relationship is
304 representative of the other times of a diurnal cycle. To address this question, we use the LAASO
305 data to examine its diurnal dependence. We chose the $w_{crit} = 0$ m/s for determining the $\overline{w_b}$ because,
306 as noted above, using an ad-hoc w_{crit} , say 0.5 m/s, leads to a markedly positive $\overline{w_b}$ for zero
307 $(TKE_M^w)^{1/2}$. By using $w_{crit} = 0$ m/s, we can force the best-fit line through the origin through the
308 least-square algorithm, freeing us from the unphysical meaning of positive intercepts. Figure 4a
309 and b show the scatterplots of the $\overline{w_b}$ versus $(TKE_M^w)^{1/2}$ in different local times simulated by WRF
310 and SAM, respectively. Both models show notably significant correlations between the two
311 quantities in different phases of a diurnal cycle, confirming the ability of $(TKE_M^w)^{1/2}$ to explain the
312 variability of $\overline{w_b}$. More importantly, the slope of the relationship varies little with local time,
313 except in the early morning and late afternoon (Fig. 4c and d). In the early morning, the stronger
314 capping inversion weakens the speeds of rising thermals when they penetrating into the inversion,
315 leading to smaller $\overline{w_b}$ for given sub-cloud turbulence (Fig. S1c). Such a stabilization effect
316 becomes less influential as the convection kicks up, which lessens the inversion strength. In the
317 late afternoon, as the solar insolation weakens, the surface fluxes decrease considerably whereas
318 the boundary layer remains deep (Fig. S1d). This leads to a decoupling between the ShCu and the
319 surface (Stull, 2012), which may explain the flatter slope between $\overline{w_b}$ and $(TKE_M^w)^{1/2}$ in the late
320 afternoon.

321 In summary, the diurnal dependence of the coupling between the w_b and sub-cloud turbulence
322 is small, except in the early morning and late afternoon when the strong capping inversion and
323 cloud-surface decoupling may lead to flatter slopes, respectively.



324

325 **Figure 4:** Scatterplots of $\overline{w_b}$ ($w_{crit} = 0$ m/s) versus the $(TKE_{ML}^w)^{1/2}$ grouped by the local
 326 standard time, simulated by WRF (a) and SAM (b). Each group of points corresponds to a best-
 327 fit linear regression line forced through zero. The slopes of the best-fit lines are plotted in (c) and
 328 (d) for WRF and SAM, respectively.

329 5. Conclusion

330 This study examines the relationship between the sub-cloud turbulence and cloud base
 331 updrafts using Doppler lidar (DL) observations of 128 shallow cumulus (ShCu) ensembles over
 332 the Southern Great Plains. We proposed a new DL sampling method that allows measuring the
 333 cloud-base updrafts for an ensemble, instead of individual, ShCu. Specifically, we take advantage
 334 of the stationarity and ergodicity of ShCu-topped boundary layers in the early afternoon when the
 335 temporal change in the surface forcing is minimum. For each ShCu case, we selected a 2-hour
 336 window of DL that includes an average amount of ~ 20 individual cumuli with varying sizes,
 337 constituting an ensemble. This allows us to compute the ensemble-averaged quantities from DL

338 measurements made at a fixed point. By analyzing the 128 ShCu ensembles, we found that the
339 vertical velocity variance explains ~ 50% variability of ensemble-mean cloud-base updrafts, thus
340 supporting the widely-held hypothesis and practice of using the sub-cloud turbulent kinetic energy
341 to parameterize the cloud-base updrafts in some state-of-the-art mass flux closure schemes of
342 convection parameterization (Bretherton et al., 2004; Neggers et al., 2009; Fletcher and Bretherton,
343 2010). To our knowledge, this is the first observational evidence that demonstrates the ability of
344 sub-cloud turbulence intensity to dictate the cloud-base updrafts.

345 With the observational data, we derived empirical relationships between the square-root of
346 sub-cloud turbulent kinetic energy and ensemble-mean cloud-base updraft speeds that are
347 computed for different thresholds of vertical velocity and by different averaging schemes.
348 Although all the 128 cases were sampled in the early afternoon, the diurnal variation of the
349 relationship is weak (except in the early morning and late afternoon), as shown by the LES
350 simulations of 18 ShCu cases over the SGP. These empirical formulas are useful for the
351 developments of cumulus parameterizations, theoretical studies of ShCu dynamics, and satellite-
352 based inference of cloud-base updrafts.

353

354

355 **Acknowledgments**

356 This study is supported by the Department of Energy (DOE) Atmospheric System Research
357 program (DE-SC0018996). The ground-based data in this study are available from the website of
358 ARM Climate Research Facility (www.archive.arm.gov/data). The LASSO data are available from
359 www.archive.arm.gov/lassobrowser. We thank the LASSO staff for maintaining the data in a user-
360 friendly way.

361

362

363

364 **References:**

- 365 Arakawa, A., & Schubert, W. H. (1974). Interaction of a cumulus cloud ensemble with the large-scale
366 environment, Part I. *Journal of the Atmospheric Sciences*, 31(3), 674-701.
- 367 Betts, A. (1973). Non-precipitating cumulus convection and its parameterization. *Quarterly Journal of the*
368 *Royal Meteorological Society*, 99(419), 178-196.
- 369 Bretherton, C. S., McCaa, J. R., & Grenier, H. (2004). A new parameterization for shallow cumulus
370 convection and its application to marine subtropical cloud-topped boundary layers. Part I:
371 Description and 1D results. *Monthly Weather Review*, 132(4), 864-882.
- 372 Brown, J. M. (1979). Mesoscale unsaturated downdrafts driven by rainfall evaporation: A numerical study.
373 *Journal of the Atmospheric Sciences*, 36(2), 313-338.
- 374 Donner, L. J., O'Brien, T. A., Rieger, D., Vogel, B., & Cooke, W. F. (2016). Are atmospheric updrafts a
375 key to unlocking climate forcing and sensitivity? *Atmospheric Chemistry and Physics*, 16(20),
376 12983-12992. <Go to ISI>://WOS:000386665800002
- 377 Fletcher, J. K., & Bretherton, C. S. (2010). Evaluating boundary layer-based mass flux closures using
378 cloud-resolving model simulations of deep convection. *Journal of the Atmospheric Sciences*, 67(7),
379 2212-2225.
- 380 Grant, A., & Brown, A. (1999). A similarity hypothesis for shallow-cumulus transports. *Quarterly Journal*
381 *of the Royal Meteorological Society*, 125(558), 1913-1936.
- 382 Grell, G. A. (1993). Prognostic evaluation of assumptions used by cumulus parameterizations. *Monthly*
383 *Weather Review*, 121(3), 764-787.
- 384 Grosvenor, D. P., Sourdeval, O., Zuidema, P., Ackerman, A., Alexandrov, M. D., Bennartz, R., et al. (2018).
385 Remote sensing of droplet number concentration in warm clouds: A review of the current state of
386 knowledge and perspectives. *Reviews of Geophysics*, 56(2), 409-453.
- 387 Kain, J. S., & Fritsch, J. M. (1993). Convective parameterization for mesoscale models: The Kain-Fritsch
388 scheme. In *The representation of cumulus convection in numerical models* (pp. 165-170): Springer.
- 389 Krishnamurti, T. N., Low-Nam, S., & Pasch, R. (1983). Cumulus parameterization and rainfall rates II.
390 *Monthly Weather Review*, 111(4), 815-828.
- 391 Lareau, N. P., Zhang, Y., & Klein, S. A. (2018). Observed boundary layer controls on shallow cumulus at
392 the ARM Southern Great Plains site. *Journal of the Atmospheric Sciences*, 75(7), 2235-2255.
- 393 Lensky, I., & Rosenfeld, D. (2006). The time-space exchangeability of satellite retrieved relations between
394 cloud top temperature and particle effective radius.
- 395 Li, Z., Rosenfeld, D., & Fan, J. (2017). *Aerosols and their Impact on Radiation, Clouds, Precipitation &*
396 *Severe Weather Events*. Retrieved from
- 397 Moeng, C.-H. (1984). A large-eddy-simulation model for the study of planetary boundary-layer turbulence.
398 *Journal of the Atmospheric Sciences*, 41(13), 2052-2062.
- 399 Neggers, R., Stevens, B., & Neelin, J. (2007). Variance scaling in shallow-cumulus-topped mixed layers.
400 *Quarterly Journal of the Royal Meteorological Society: A journal of the atmospheric sciences,*
401 *applied meteorology and physical oceanography*, 133(628), 1629-1641.
- 402 Neggers, R., Stevens, B., & Neelin, J. D. (2006). A simple equilibrium model for shallow-cumulus-topped
403 mixed layers. *Theoretical and Computational Fluid Dynamics*, 20(5-6), 305-322.
- 404 Neggers, R. A., Köhler, M., & Beljaars, A. C. (2009). A dual mass flux framework for boundary layer
405 convection. Part I: Transport. *Journal of the Atmospheric Sciences*, 66(6), 1465-1487.
- 406 Rasp, S., Schulz, H., Bony, S., & Stevens, B. (2019). Combining crowd-sourcing and deep learning to
407 explore the meso-scale organization of shallow convection. *arXiv preprint arXiv:1906.01906*.
- 408 Reutter, P., Su, H., Trentmann, J., Simmel, M., Rose, D., Gunthe, S., et al. (2009). Aerosol-and updraft-
409 limited regimes of cloud droplet formation: influence of particle number, size and hygroscopicity
410 on the activation of cloud condensation nuclei (CCN). *Atmospheric Chemistry and Physics*, 9(18),
411 7067-7080.
- 412 Rogers, R., & Yau, M. K. (1996). *A short course in cloud physics*: Elsevier.

- 413 Romps, D. M. (2014). An analytical model for tropical relative humidity. *Journal of Climate*, 27(19), 7432-
414 7449.
- 415 Rosenfeld, D. (2014). Climate effects of aerosol-cloud interactions. *Science*, 1247490(379), 343.
- 416 Rosenfeld, D., Fischman, B., Zheng, Y., Goren, T., & Giguzin, D. (2014). Combined satellite and radar
417 retrievals of drop concentration and CCN at convective cloud base. *Geophysical Research Letters*,
418 41(9), 3259-3265.
- 419 Rosenfeld, D., Zheng, Y., Hashimshoni, E., Pöhlker, M. L., Jefferson, A., Pöhlker, C., et al. (2016). Satellite
420 retrieval of cloud condensation nuclei concentrations by using clouds as CCN chambers.
421 *Proceedings of the National Academy of Sciences*, 201514044.
- 422 Rosenfeld, D., Zhu, Y., Wang, M., Zheng, Y., Goren, T., & Yu, S. (2019). Aerosol-driven droplet
423 concentrations dominate coverage and water of oceanic low-level clouds. *Science*, 363(6427),
424 eaav0566.
- 425 Seinfeld, J. H., Bretherton, C., Carslaw, K. S., Coe, H., DeMott, P. J., Dunlea, E. J., et al. (2016). Improving
426 our fundamental understanding of the role of aerosol– cloud interactions in the climate system.
427 *Proceedings of the National Academy of Sciences*, 113(21), 5781-5790.
- 428 Stevens, B. (2006). Bulk boundary-layer concepts for simplified models of tropical dynamics. *Theoretical
429 and Computational Fluid Dynamics*, 20(5-6), 279-304.
- 430 Stevens, B. (2007). On the growth of layers of nonprecipitating cumulus convection. *Journal of the
431 Atmospheric Sciences*, 64(8), 2916-2931.
- 432 Stull, R. B. (2012). *An introduction to boundary layer meteorology* (Vol. 13): Springer Science & Business
433 Media.
- 434 Teschke, G., & Lehmann, V. (2017). Mean wind vector estimation using the velocity–azimuth display
435 (VAD) method: an explicit algebraic solution. *Atmospheric Measurement Techniques*, 10(9), 3265.
- 436 Twomey, S. (1959). The nuclei of natural cloud formation part II: The supersaturation in natural clouds and
437 the variation of cloud droplet concentration. *Geofisica pura e applicata*, 43(1), 243-249.
- 438 van Stratum, B. J., Vilá-Guerau de Arellano, J., van Heerwaarden, C. C., & Ouwersloot, H. G. (2014).
439 Subcloud-layer feedbacks driven by the mass flux of shallow cumulus convection over land.
440 *Journal of the Atmospheric Sciences*, 71(3), 881-895.
- 441 Zhang, Y., & Klein, S. A. (2013). Factors controlling the vertical extent of fair-weather shallow cumulus
442 clouds over land: Investigation of diurnal-cycle observations collected at the ARM Southern Great
443 Plains site. *Journal of the Atmospheric Sciences*, 70(4), 1297-1315.
- 444 Zheng, Y. (2019). Theoretical understanding of the linear relationship between convective updrafts and
445 cloud-base height for shallow cumulus clouds. Part I: Maritime conditions. *Journal of the
446 Atmospheric Sciences*(2019).
- 447 Zheng, Y., & Rosenfeld, D. (2015). Linear relation between convective cloud base height and updrafts and
448 application to satellite retrievals. *Geophysical Research Letters*, 42(15), 6485-6491. <Go to
449 ISI>://WOS:000360414900044
- 450 Zheng, Y., Rosenfeld, D., & Li, Z. (2015). Satellite inference of thermals and cloud-base updraft speeds
451 based on retrieved surface and cloud-base temperatures. *Journal of the Atmospheric Sciences*, 72(6),
452 2411-2428.
- 453 Zheng, Y., Rosenfeld, D., & Li, Z. (2016). Quantifying cloud base updraft speeds of marine stratocumulus
454 from cloud top radiative cooling. *Geophysical Research Letters*, 43(21).
- 455 Zheng, Y., Sakradzija, M., Lee, S.-S., & Li, Z. (2020). Theoretical understanding of the linear relationship
456 between convective updrafts and cloud-base height for shallow cumulus clouds. Part II: Continental
457 conditions. *Journal of the Atmospheric Sciences*, 77(4), 1313-1328.

458

459

1
2
3
4
5
6
7
8
9
10
11
12
13
14
15
16
17
18
19
20
21
22
23

Geophysical Research Letters

Supporting Information for

Sub-cloud turbulence explains cloud-base updrafts for shallow cumulus ensembles: First observational evidence

Youtong Zheng¹, Daniel Rosenfeld², and Zhanqing Li¹

Affiliations:

¹Earth System Science Interdisciplinary Center, University of Maryland, College Park, Maryland, 20742, USA.

²Institute of Earth Science, Hebrew University of Jerusalem, Jerusalem, Israel.

Contents of this file

1. Text S1~S2
2. Figures S1~S4
3. Table S1

24

25 **Text S1: LASSO data**

26 The Large-Eddy Simulation (LES) Atmospheric Radiation Measurements (ARM) Symbiotic
27 Simulation and Observation (LASSO) project was launched in 2015 by the U.S. Department of
28 Energy’s ASR program (Gustafson Jr et al., 2020). Routine large-eddy simulations of shallow
29 convection at ARM’s SGP observatory were conducted between 2015 and 2019. One of the core
30 concepts of LASSO is to provide a library of ShCu cases for researchers to conduct composite
31 analysis with statistical robustness. This contrasts with previous LES studies that are limited to
32 only a couple of ShCu cases. In this study, we use all the 18 ShCu cases released in the first two
33 phases (2015 and 2016) of the LASSO. The output from two different models are used: Weather
34 Research and Forecasting (WRF) (Skamarock et al., 2008) and System for Atmospheric Modeling
35 (SAM) (Khairoutdinov and Randall, 2003). Both models were run with resolutions of 100 m in
36 the horizontal and 30 m in the vertical within a domain with a size of 14.4 km. The initial state and
37 the forcing data are the same: balloon-based sounding used as the initial state, large-scale-forcing
38 input obtained from the European Centre for Medium-Range Weather Forecasts (ECMWF)
39 analysis averaged over the spatial scale of 114 km, and the homogenized surface fluxes obtained
40 from the ARM Variational Analysis (VARANAL) product. The WRF model used in this study
41 adopted LASSO-Morrison cloud microphysical scheme (Gustafson et al., 2017) whereas the SAM
42 uses the two-moment Bulk scheme (Morrison et al., 2005). Here, we offer additional discussions
43 on two aspects of the LASSO data. First, one may suspect if the horizontal resolution of 100 m is
44 fine enough for studying the vertical velocity (Guo et al., 2008; Donner et al., 2016; Endo et al.,
45 2019). Since this study is focused on the ensemble-averaged vertical velocity, this resolution issue
46 is more or less alleviated. Improving the horizontal resolution to 25 m has a discernable, but not
47 significant, influence on the domain-averaged vertical velocity statistics (Endo et al., 2019).
48 Second, the selection of the specific combinations of large-scale and surface forcing data is purely
49 random. There is no conclusive evidence as to which combination of forcing is superior to others.

50 We determine the cloud-base height (z_b) as the altitude with the largest cloud cover. At the z_b ,
51 we selected cloudy pixels with liquid water greater than 0.01 g m^{-3} to compute the cloud-base
52 updrafts. The averaging routines are the same as those described in Section 3 of the main
53 manuscript. The TKE_{ML} is computed as $0.5 * (u'^2 + v'^2 + w'^2)$ averaged below the z_b . The

54 mixed-layer height, h , is determined as the altitude with the most negative buoyancy fluxes. The
55 convective time scale, t^* , is computed as $h/(TKE_{ML})^{1/2}$.

56

57 **Text S2: Comparison between the DL- and LAASO-derived results**

58 As shown in Figure 3a and S4c, d and summarized in Table S1, WRF and SAM show ~ 50%
59 steeper slope of the relationships between the $\overline{w_b}$ and $(TKE_M^w)^{1/2}$ than that from the DL. We think
60 that the larger slope is likely due to the known problem of LES in overestimating the updrafts near
61 cloud bases (Endo et al., 2019). As shown in Endo et al., (2019), compared with DL observations,
62 the LES tends to shift the probability density function (PDF) of cloud-base vertical velocities
63 toward the positive end. This leads to weaker downdrafts and stronger updrafts at cloud bases.
64 This problem is found to be a consequence of model physics underestimating the evaporative and
65 radiative cooling near cloud bases, processes driving downdrafts. It's reasonable to conjecture that
66 such an effect should be less influential for weaker sub-cloud forcing. As a thought experiment,
67 one may imagine the evaporative cooling to approach zero as the convection gradually shuts off,
68 leaving little chance for the underestimated evaporative cooling to modify the $\overline{w_b}$.

69

70

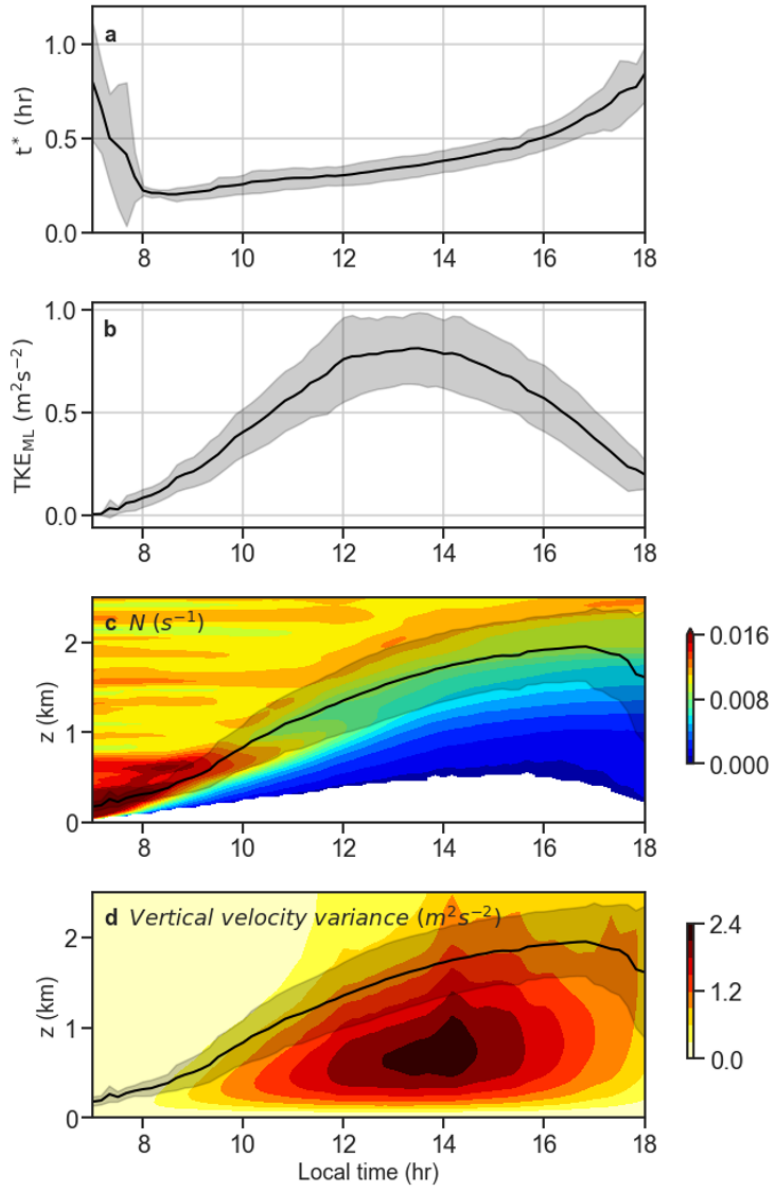
71

72

73

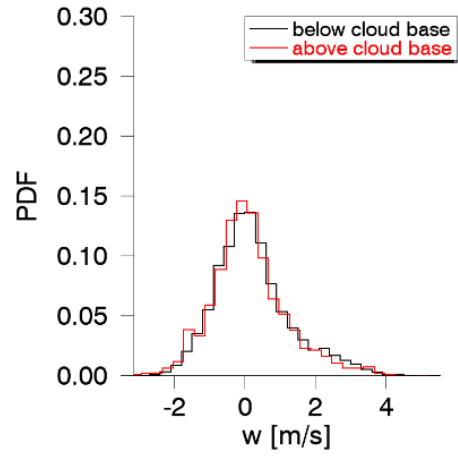
74

75



76

77 **Figure S1:** WRF-simulated composite diurnal variations of t^* (a), TKE_{ML} (b), and height-time
 78 plots of Brunt-Vaisala frequency (c), and vertical velocity variance (d). In (c) and (d), the black
 79 lines mark the diagnosed mixed-layer height (h). All plotted are the composite means of the 18
 80 ShCu cases from the 1st phase of the LAASO project.



81

82

Figure S2: Probability density functions of vertical velocity for pixels at 100 m below
(black) and above (red) the cloud bases.

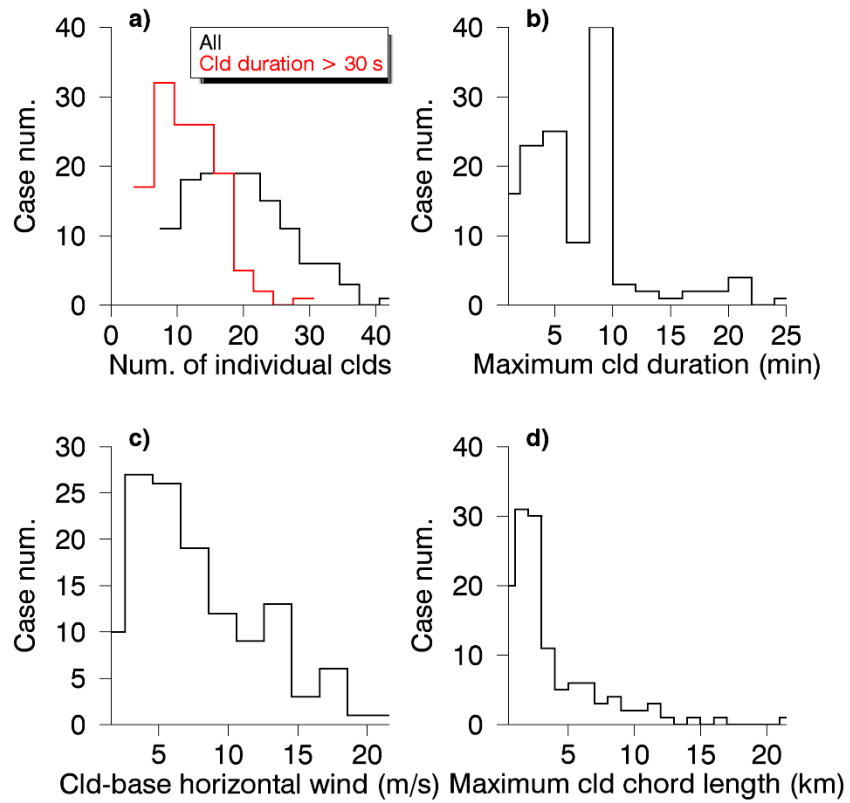
83

84

85

86

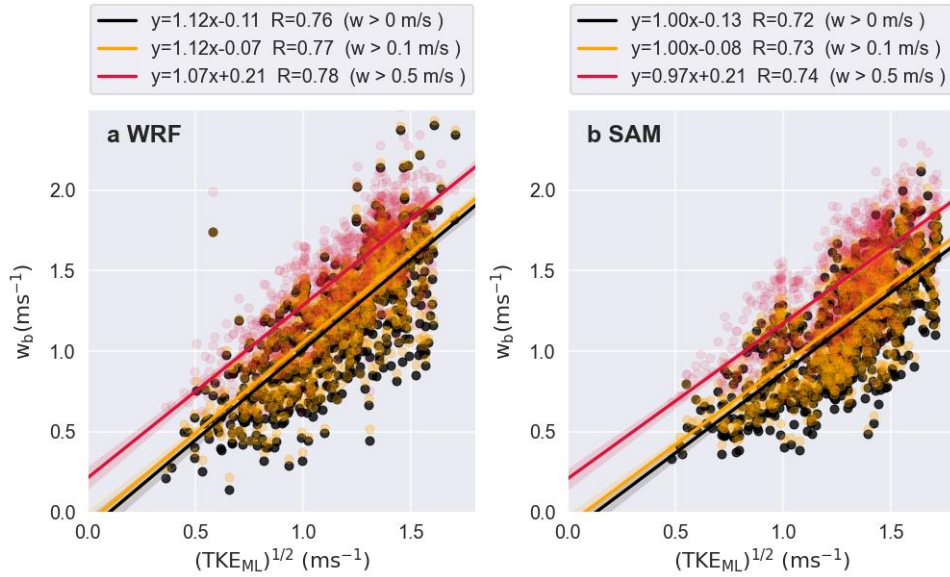
87



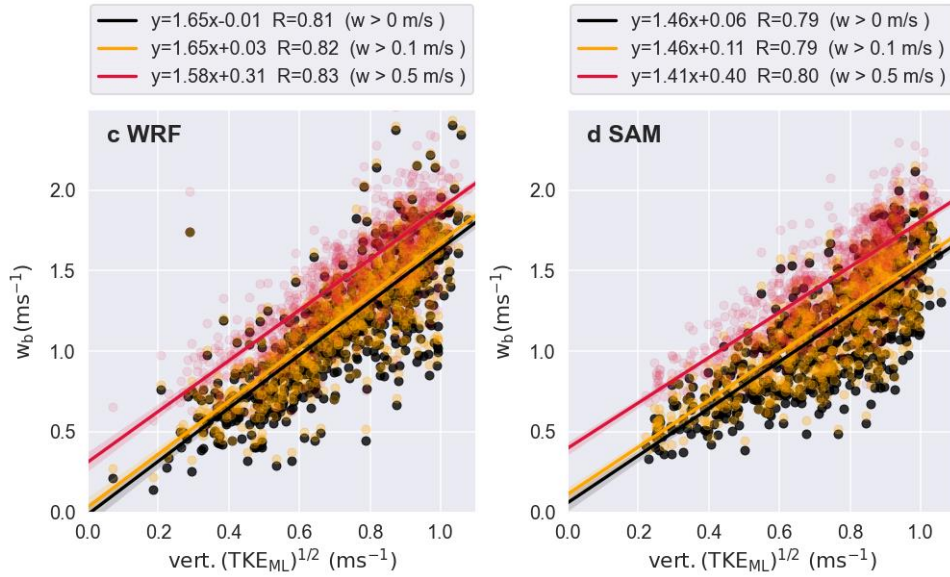
88

89 **Figure S3:** Statistical distribution of key quantities for the 128 ShCu cases including (a) the
 90 number of individual cumuli (the red marks those that last longer than 30 secs), (b) maximum
 91 cloud duration, (c) horizontal wind speed near cloud base, and (d) maximum cloud chord length.

92



93



94

95 **Figure S4:** Scatter plots of simulated $\overline{w_b}$ versus $(TKE_{ML})^{1/2}$ (upper) and $(TKE^w_{ML})^{1/2}$

96 (bottom), simulated by WRF (left) and SAM (right).

97

98

99

100

	Slope	Intercept (m/s)	Slope (forced through origin)	Corr.
DL $\overline{w_b}$ ($w > 0$ m/s)	1.04 ± 0.09	0.11 ± 0.06	1.20	0.73
DL $\overline{w_b}$ ($w > 0.1$ m/s)	1.04 ± 0.09	0.20 ± 0.06	N/A	0.73
DL $\overline{w_b}$ ($w > 0.5$ m/s)	0.98 ± 0.10	0.61 ± 0.07	N/A	0.68
DL $\overline{w_b^{vol}}$ ($w > 0$ m/s)	1.81 ± 0.15	0.22 ± 0.10	2.11	0.74
DL $\overline{w_b^{vol}}$ ($w > 0.1$ m/s)	1.80 ± 0.15	0.24 ± 0.10	N/A	0.74
DL $\overline{w_b^{vol}}$ ($w > 0.5$ m/s)	1.64 ± 0.14	0.50 ± 0.10	N/A	0.71
WRF $\overline{w_b}$ ($w > 0$ m/s)	1.65 ± 0.04	-0.04 ± 0.03	1.63	0.81
WRF $\overline{w_b}$ ($w > 0.1$ m/s)	1.65 ± 0.04	0.03 ± 0.03	N/A	0.82
WRF $\overline{w_b}$ ($w > 0.5$ m/s)	1.58 ± 0.04	0.31 ± 0.03	N/A	0.83
SAM $\overline{w_b}$ ($w > 0$ m/s)	1.46 ± 0.04	0.06 ± 0.03	1.54	0.79
SAM $\overline{w_b}$ ($w > 0.1$ m/s)	1.46 ± 0.04	0.11 ± 0.03	N/A	0.79
SAM $\overline{w_b}$ ($w > 0.5$ m/s)	1.41 ± 0.04	0.40 ± 0.03	N/A	0.80

Table S1: Statistics of the relationships between the ensemble-mean cloud-base updrafts and

$(\text{TKE}_{\text{ML}}^w)^{1/2}$ derived from DL, WRF, and SAM data.

101
102
103
104
105
106
107
108
109
110
111
112
113
114

115 **Reference:**

- 116 Donner, L. J., O'Brien, T. A., Rieger, D., Vogel, B., & Cooke, W. F. (2016). Are atmospheric
117 updrafts a key to unlocking climate forcing and sensitivity? *Atmospheric Chemistry and*
118 *Physics*, *16*(20), 12983-12992. <Go to ISI>://WOS:000386665800002
- 119 Endo, S., Zhang, D., Vogelmann, A. M., Kollias, P., Lamer, K., Oue, M., et al. (2019). Reconciling
120 differences between large-eddy simulations and Doppler lidar observations of continental
121 shallow cumulus cloud-base vertical velocity. *Geophysical Research Letters*, *46*(20),
122 11539-11547.
- 123 Guo, H., Liu, Y., Daum, P. H., Senum, G. I., & Tao, W.-K. (2008). Characteristics of vertical
124 velocity in marine stratocumulus: comparison of large eddy simulations with observations.
125 *Environmental Research Letters*, *3*(4), 045020.
- 126 Gustafson Jr, W. I., Vogelmann, A. M., Li, Z., Cheng, X., Dumas, K. K., Endo, S., et al. (2020).
127 The Large-Eddy Simulation (LES) Atmospheric Radiation Measurement (ARM)
128 Symbiotic Simulation and Observation (LASSO) Activity for Continental Shallow
129 Convection. *Bulletin of the American Meteorological Society*, *101*(4), E462-E479.
- 130 Gustafson, W. I., Vogelmann, A. M., Cheng, X., Endo, S., Krishna, B., Li, Z., et al. (2017).
131 *Recommendations for the implementation of the LASSO workflow*. Retrieved from
- 132 Khairoutdinov, M. F., & Randall, D. A. (2003). Cloud resolving modeling of the ARM summer
133 1997 IOP: Model formulation, results, uncertainties, and sensitivities. *Journal of the*
134 *Atmospheric Sciences*, *60*(4), 607-625.
- 135 Morrison, H., Curry, J., & Khvorostyanov, V. (2005). A new double-moment microphysics
136 parameterization for application in cloud and climate models. Part I: Description. *Journal*
137 *of the Atmospheric Sciences*, *62*(6), 1665-1677.
- 138 Skamarock, W. C., Klemp, J. B., Dudhia, J., Gill, D. O., Barker, D. M., Duda, M. G., et al. (2008).
139 *G.: A description of the Advanced Research WRF version 3*. Paper presented at the NCAR
140 Tech. Note NCAR/TN-475+ STR.

141
142